IOP Publishing New J. Phys. 26 (2024) 053042 https://doi.org/10.1088/1367-2630/ad4abc

New Journal of Physics
The open access journal at the forefront of physics

Deutsche Physikalische Gesellschaft DPG
IOP Institute of Physics

Published in partnership with: Deutsche Physikalische Gesellschaft and the Institute of Physics

CrossMark

OPEN ACCESS

RECEIVED
26 January 2024

REVISED
25 April 2024

ACCEPTED FOR PUBLICATION
13 May 2024

PUBLISHED
28 May 2024

Original content from this work may be used under the terms of the Creative Commons Attribution 4.0 licence.

Any further distribution of this work must maintain attribution to the author(s) and the title of the work, journal citation and DOI.

PAPER

Long-range pairing in monolayer $NbSe_2$ facilitates the emergence of topological superconducting states

Y Z Li[1,*], Q Gao[1], Y R Li[1,3], J X Zhong[2,3,*] and L J Meng[1,3,*]

[1] School of Physics and Optoelectronics, Xiangtan University, Xiangtan 411105, Hunan, People's Republic of China
[2] Center for Quantum Science and Technology, Department of Physics, Shanghai University, Shanghai 200444, People's Republic of China
[3] Hunan Key Laboratory for Micro-Nano Energy Materials and Devices, Xiangtan 411105, Hunan, People's Republic of China
[*] Authors to whom any correspondence should be addressed.

E-mail: 202031000131@smail.xtu.edu.cn, jxzhong@xtu.edu.cn and ljmeng@xtu.edu.cn

Keywords: long-range-neighboring superconducting pairing, topological superconducting states under zero magnetic field, functional renormalization group approach

Abstract

The paper systematically study topological superconducting (TSC) phases in monolayer $NbSe_2$ by constructing the hybrid paring tight-binding model of mixing on-site *s*-wave pairing (p_s) and long-range pairing (p_{A1}) for the first time. We observe rich phases with both fixed and sensitive Chern numbers (CNs) depending on the chemical potential (μ) and out-of-plane magnetic field (V_z). As p_{A1} increases, the TSC phase manifests matching and mismatching features according to whether the CNs match with the number of topological edge states (TESs). Strikingly, the introduction of long-range pairing significantly reduces the critical V_z to form TSC phases compared with the pure on-site *s*-wave paring. Moreover, the TSC phases can be modulated even at $V_z = 0$ under appropriate μ and p_{A1}, which is identified by the robust TESs of ribbons. Additionally, the long-range pairing influences the hybridization of bulk and edge states, resulting in a matching/mismatching bulk-boundary correspondence with localized/oscillating TESs on the ribbons. Our findings are helpful for realizing TSC states through compressive strain experimentally to strengthen long-range pairings, as well as designing and regulating TSC materials.

1. Introduction

Topological superconductors are extensively studied with the aim of inducing and manipulating Majorana zero modes, which is crucial for realizing topological quantum information due to non-Abelian statistical property [1–7]. Recently discovered transition metal dichalcogenides are excellent candidates to host topological superconductivity. For example, Ising superconductor 1 T_d-$PdSe_2$ is detected large in-plane critical field more than 7 times that of the Pauli limit [8], heavily gated MoS_2, supporting the exotic spin-singlet $p + ip$-wave pairing in the presence of Ising SOC and Rashba SOC, is a topological superconducting (TSC) phase that breaks time-reversal symmetry spontaneously and possesses nonzero Chern numbers (CNs) [9], 2 M-WS_2 presents a transition temperature $T_c = 8.8$ K and intrinsic superconductivity [10], 2 H-$NbSe_2$ with SOC takes the lead as an intrinsic superconductor that exhibits superconductivity and charge-density wave phase from bulk to monolayer and withstands exceptionally high magnetic fields far beyond the Pauli limit for superconductivity [11–14], and so forth.

Previous studies demonstrated that one of formation mechanism of TSC may arises from a combination of out-of-plane ferromagnetism, superconductivity and Rashba-type spin–orbit coupling (RSOC) [15–17]. Two-dimensional TSCs with nontrivial properties exhibit topological edge states (TESs) along their edges, as dictated by the well-established bulk-boundary correspondence (BBC) principle, which associates the topological invariant with the number of TESs [2, 18]. However, recent research progress on topological materials has revealed the sensitivity and richness of the CN phase diagram to variations in the chemical

© 2024 The Author(s). Published by IOP Publishing Ltd on behalf of the Institute of Physics and Deutsche Physikalische Gesellschaft

potential (μ), magnetic field (V_z), and superconducting order parameter amplitude [19–23]. Furthermore, there is evidence of a mismatch between the CN and the number of TESs, indicating a deviation from the BBC principle [19, 21–30]. For example, 2 H_b-stacked bilayer transition metal dichalcogenides and bilayer bismuth lattice considering on-site *s*-wave pairing with Kane–Mele type SOC strength 0.0075 eV or without SOC show the TSC phases with rich and high CNs up to 4 under various μ and superconducting order parameters, which do not strictly always contain the same number of TESs as the CNs [19, 25, 29]. 2D square lattice of tetragonal D_{4h} symmetry with a mixture of on-site and off-site singlet pairing manifests non-trivial high CN, massive edge states, and zero energy modes out of high symmetry points, and the number of zero-energy modes is higher than the CN in certain cases under SOC (the strength of SOC equal to pairing) and various V_z [23]. A checkerboard-lattice model without SOC combining the Chern insulator and chiral *p*-wave superconductivity produces TSC with non-zero CNs, and the results clearly reveal the mismatch between the CNs and TESs [28]. Previous studies indicate that, in certain cases, the CNs and TESs of two-dimensional TSC do not always agree with the BBC principle. And pioneering studies show another possible formation mechanism of TSC is originate from the combination of RSOC and unconventional long-range pairing [23, 26–28]. However, the effect of long-range pairing on the formation of TSC for monolayer $NbSe_2$ still lacks and requires comprehensive investigation.

In our work, we use projection operator approach [31] for 2 H-$NbSe_2$ with C_{6v} point group symmetry to obtain long-range (including nearest-neighbor (NN), next-nearest-neighbor (NNN), third-nearest-neighbor (TNN)) pairing function of irreducible representation A_1. Different from just considering the conventional on-site *s*-wave pairing in previous studies [15], we here investigate systematically rich TSC phases by considering a novel hybrid pairing of on-site *s*-wave Δ_s and long-range off-site Δ_{A1} in monolayer $NbSe_2$. The specific form of hybrid pairing is presented in equations (6)–(9). This exploration is conducted by applying external out-of-plane V_z and RSOC based on a Bogoliubov–de Gennes (BdG) Hamiltonian. To study topological properties of TSC phase, we initially employ efficient method [32] to compute CN as a function of μ and V_z. The value of V_z lies in [0.0, 0.1]eV which is accessible by external magnetic field in experiment or by constructing heterojunction with two-dimensional ferromagnet (CrX_3, X=Cl, Br, I) [15]. The essential point is that the TSC phases with non-zero CN can be regulated under zero V_z, and consequently loosening the constraint on the formation of TSC. Subsequently, we calculate the TESs of zigzag and armchair ribbons to confirm TSC states of CNs phase diagram. Additionally, we investigate the effect of the NN pairing potential on the bulk state and explicitly demonstrate the mismatches between the bulk CNs and TESs by calculating the bulk band-gap between conduction band and valance band. It becomes evident that bulk states hybridize with edge states when the band-gap is tiny, leading to a mismatch between CNs and TESs. Finally, we present the probability possibility distribution ($|\psi(n)|^2$) in real space to reveal the distribution of TESs.

2. Methods and model

The *d*-orbitals of the Nb atoms in monolayer $NbSe_2$ dominating the energy bands near the Fermi level E_F suggest that the superconductivity is primarily contributed by the Nb-4d bands [33]. Therefore the tight-binding Hamiltonian of monolayer $NbSe_2$ must meet the symmetry requirements of the triangular sublattice of Nb atoms (point group: C_{6v}) [11, 33, 34]. Figure 1(a) shows the trigonal lattice of Nb atoms and the zigzag/armchair ribbons width N_z and N_a in monolayer $NbSe_2$. Considering a novel hybrid pairing term H_{SC}, the tight-binding Hamiltonian defined on a triangular lattice becomes [15]

$$H = H_t + H_{\mathrm{RSOC}} + H_{\mathrm{M}} + H_{\mathrm{SC}} \tag{1}$$

$$\begin{aligned} H_t &= -\sum_{i,j,\sigma} t_{ij} c^{\dagger}_{i\sigma} c_{j\sigma} - \mu \sum_{i,\sigma} c^{\dagger}_{i\sigma} c_{i\sigma} \\ &= -\sum_{i,j} t_{ij} \left(c^{\dagger}_{i\uparrow} c_{j\uparrow} + c^{\dagger}_{i\downarrow} c_{j\downarrow} \right) - \mu \sum_{i} \left(c^{\dagger}_{i\uparrow} c_{i\uparrow} + c^{\dagger}_{i\downarrow} c_{i\downarrow} \right) \end{aligned} \tag{2}$$

$$H_{\mathrm{RSOC}} = i\alpha_R \sum_{\langle i,j\rangle,\sigma\sigma'} \left[\mathbf{e}_z \cdot \left(\mathbf{e}_{ij} \times \boldsymbol{\sigma} \right) \right]^{\sigma\sigma'} c^{\dagger}_{i\sigma} c_{j\sigma'} = i\alpha_R \sum_{\langle i,j\rangle,\sigma\sigma'} \left[e^x_{ij}\sigma_y - e^y_{ij}\sigma_x \right]^{\sigma\sigma'} c^{\dagger}_{i\sigma} c_{j\sigma'} \tag{3}$$

$$H_{\mathrm{M}} = -\sum_{i,\sigma,\sigma'} \left[\boldsymbol{V_Z}(i) \cdot \boldsymbol{\sigma} \right]^{\sigma\sigma'} c^{\dagger}_{i\sigma} c_{i\sigma'} = -\sum_{i,\sigma,\sigma'} \left[V_Z \sigma_Z \right]^{\sigma\sigma'} c^{\dagger}_{i\sigma} c_{i\sigma'} \tag{4}$$

$$H_{\mathrm{SC}} = \sum_{\langle i,j\rangle} \Delta_{ij} \left(c^{\dagger}_{i\uparrow} c^{\dagger}_{j\downarrow} + H.c. \right) \tag{5}$$

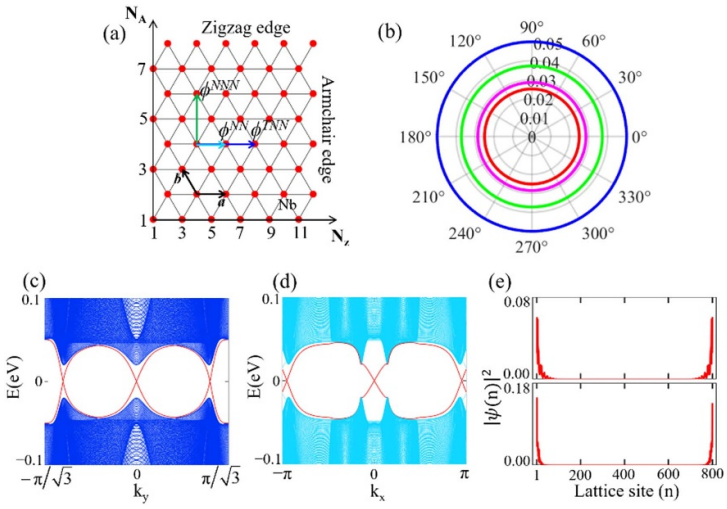

Figure 1. (a) The trigonal lattice of Nb atoms and zigzag/armchair ribbon with width N_Z/N_A. Lattice constant $a = b$ is set 1. The cyan/green/blue arrows denote the initial projection vector of NN/NNN/TNN pairing. (b) The distribution of long-range pairing function with θ. Blue/green/pick/red represents pure s-wave/NN/NNN/TNN pairing, respectively. (c)(d) Edge spectra for (c) zigzag and (d) armchair ribbons with 800 lattice sites under $\mu = -0.272$ eV, respectively. (e) The upper and lower panels are the probability distributions on edges around the Fermi level (E_F) for zigzag (c) and armchair (d) ribbons.

where H_t is the hopping term, the t_{ij} corresponds to the hopping amplitudes from j to i and μ is the chemical potential. H_{RSOC} represents the Rashba SOC with strength α_R. H_{M} is out-of-plane magnetic field with strength V_z. Instead of just considering the on-site s-wave pairing [15], the H_{SC} describes novel hybrid superconducting pairing, where $i = j$ represents on-site (s-wave) pairing and $i \neq j$ indicates neighboring pairing which is a long-range pairing term considered in our manuscript. Moreover, introducing percentage parameter, the ratio of two types of pairing can be continuously changed under the fixed total magnitude of Δ_t. We use $p_s \oplus p_{\mathrm{A1}}$ to denote the mixed paring with $p_s + p_{\mathrm{A1}} = 1$, where p_s (p_{A1}) represents the percentage for s-wave Δ_s (long-range paring Δ_{A1}). Liu *et al* [27] introduces long-range pairing potential based on the projection operator approach. The trial wave functions of three neighbors (NN, NNN, TNN) (figure 1(a)) are $\phi^{\mathrm{NN}} = \delta_{i,i+x}$ and $\phi^{\mathrm{NNN}} = \delta_{i,i+\sqrt{3}y}$ and $\phi^{\mathrm{TNN}} = \delta_{i,i+2x}$, respectively. Using the character table of point group (C_{6v} for Nb sublattice), we apply the projection operator $p(A_1)$ to trial wave functions ($\phi^{\mathrm{NN}}, \phi^{\mathrm{NNN}}, \phi^{\mathrm{TNN}}$), then transform into k-space and obtain the following basis functions for the trivial representation A_1 with strength parameters p_{A1}:

$$\Delta_{\mathrm{A1_NN}}(\boldsymbol{k}) = p_{\mathrm{A1}}\Delta_t\left[\cos(k_x) + \cos\left(k_x/2 + \sqrt{3}k_y/2\right) + \cos\left(k_x/2 - \sqrt{3}k_y/2\right)\right] \tag{6}$$

$$\Delta_{\mathrm{A1_NNN}}(\boldsymbol{k}) = p_{\mathrm{A1}}\Delta_t\left[\cos\left(\sqrt{3}k_y\right) + \cos\left(3k_x/2 + \sqrt{3}k_y/2\right) + \cos\left(3k_x/2 - \sqrt{3}k_y/2\right)\right] \tag{7}$$

$$\Delta_{\mathrm{A1_TNN}}(\boldsymbol{k}) = p_{\mathrm{A1}}\Delta_t\left[\cos(2k_x) + \cos\left(k_x + \sqrt{3}k_y\right) + \cos\left(k_x - \sqrt{3}k_y\right)\right] \tag{8}$$

where $k_x = k\cos\theta$, $k_y = k\sin\theta$, $k = |\boldsymbol{k}|$, and θ is the in-plane azimuth angle. Therefore, the BdG Hamiltonian of Nb-sublattice in the Nambu basis $\psi = (c_{k\uparrow}, c_{k\downarrow}, c^{\dagger}_{-k\uparrow}, c^{\dagger}_{-k\downarrow})^T$, incorporating V_z, RSOC, s-wave and long-range pairing, is obtained as follows:

$$H(k) = \begin{bmatrix} E_t\sigma_0 + E_{R_x}\sigma_x + E_{R_y}\sigma_y + V_z\sigma_z & \mathrm{i}(\Delta_s + \Delta_{\mathrm{A1_NN}} + \Delta_{\mathrm{A1_NNN}} + \Delta_{\mathrm{A1_TNN}})\sigma_y \\ -\mathrm{i}(\Delta_s + \Delta_{\mathrm{A1_NN}} + \Delta_{\mathrm{A1_NNN}} + \Delta_{\mathrm{A1_TNN}})^*\sigma_y & -E_t\sigma_0 - E_{R_x}\sigma_x + E_{R_y}\sigma_y - V_z\sigma_z \end{bmatrix} \tag{9}$$

where E_t the hopping term E_t includes the first-/second-/third-neighboring with parameters $t_1 = -0.04$ eV/$t_2 = -0.132$ eV/$t_3 = -0.012$ eV. The RSOC term is given by E_{R_x} and E_{R_y} with strength parameter $\alpha_R = 0.1$ eV throughout the paper:

$$E_{R_x} = 2\sqrt{3}\alpha_R \sin\left(\sqrt{3}k_y/2\right)\cos(k_x/2) \tag{10}$$

$$E_{R_y} = -2\alpha_R\left[\sin(k_x) + \sin(k_x/2)\cos\left(\sqrt{3}k_y/2\right)\right]. \tag{11}$$

The bulk 2 H-$NbSe_2$ realizes an s-wave topological superconductor with CNs(3, −2, −1), and its ribbon exhibits the same number topological response in terms of TESs [15]. The superconducting pairing strength

gradually diminishes with increasing long-rang pairing distance, implying that the magnetic field strength required to achieve a TSC state is significantly reduced as shown in figure 1(b). Figures 1(c) and (d) depict the TESs of zigzag and armchair edge ribbons with CN = 3, which are in agreement with pioneering work [15]. The probability distribution$|\psi(n)|^2$ near zero-energy along the zigzag and armchair edge lattice sites manifests Majorana fermions emerging near the lattice boundary as shown in figure 1(e).

3. Results and discussion

To characterize the topological properties of TSCs, we initially calculate the CN as a function of μ and V_z for the mixed paring state of Δ_s and Δ_{A1}, as illustrated in figure 2. Previous study shows bulk $NbSe_2$, considering a pure *s*-wave superconducting pairing and RSOC, exhibits TSC states with non-zero CNs as long as V_z exceeds Δ_s under appropriate μ [15]. For 0.98⊕0.02 mixed superconducting state, monolayer $NbSe_2$ still exists three TSC phases with non-zero CNs (3, −2, −1). However, the three regions of TSC change in a non-consistent manner due to mixed effect of *s*-wave and long-range pairings, as depicted in figure 2(a). When Δ_t is 0.05, the regions with CNs = 3 and −2 are larger, while the region with CN = −1 is smaller than the pure *s*-wave pairing. When the total superconducting pairing decreases ($\Delta_t = 0.03$), the three regions with topological nontrivial CNs display the similar change trend. We present the results under total mixed superconducting pairing of 0.05 in the following calculations, unless specified otherwise. Furthermore, our findings do not change qualitatively with pairing strength if total mixed superconducting pairing is not extremely small.

As the proportion of Δ_{A1_NN} (p_{A1} of the NN) increases, the regions with CNs = 3 and −2 expand continuously, and the region with CN = −1 becomes progressively smaller. More interestingly, we clearly observe that the critical value of V_z to generate TSC phases with CNs (3, −2) decreases significantly, indicating a substantial ease of experimental difficulty for realizing TSC phases. When p_{A1} increases to 0.14, which corresponds to the first critical proportion in our calculations, the region with CN = −1 disappears under $V_z = [0.0, 0.1]$. The minimal (critical) V_z needed to form TSC phases with CN = 3(−2) is 0.017(0.003), which is significantly less than the critical V_z compared with the pure *s*-wave case as seen in figure 2(b).

Figures 2(c)–(f) show more TSC phases with non-zero CNs (e.g. CN = ±6, ±5, ±4, ±3, ±2, ±1) appearing and the TSC phase regions with CNs = 3 and −2 start to shrink when p_{A1} is greater than 0.14. The CN displays a sensitive dependence on V_z and μ and distributes irregularly between CN = 3 and CN = −2 phases due to long-range pairing, which has also been observed in previous studies [19, 20, 22, 24, 26–29]. It is notably that the sensitive non-zero CNs appear even under $V_z = 0$ when p_{A1} is greater than or equal to 0.16 (see figures 2(c)–(f), 3 and 4), suggesting that there may be more intrinsic superconductors (e.g. 1 T-$PdSe_2$ [35], 1T-$PdTe_2$ [36], 2H-TaS_2 [13], etc.) that can induce TSC phases through neighbor pairing without external V_z. Figures 2(c)–(f) display the region with sensitive CNs steadily expanding, and the trend of easy-to-vary in CNs becomes less sensitive as p_{A1} increases. When p_{A1} increases to 0.20, the region originally with CN = 3 disappears and is replaced by CN = −3. At this second critical proportion ($p_{A1} = 0.20$), the whole phase diagram mainly includes TSC phases with irregular nonzero CNs (−3, −2, 6) at $V_z = 0$ (see figure 2(f)).

When p_{A1} is greater than 0.20, the regions with CN = −3 and 6 become sensitive again as shown in figures 3(a) and (b). Moreover, the size of these regions decreases continually, and the incipient region with CN = 3 reappears, as shown in figures 3(b)–(f). As p_{A1} increases progressively to 1.00, only TSC phase with nonzero sensitive CNs near $\mu = 0$ exists in the phase diagram, and all other TSC phase regions with fixed CNs disappear, as presented in figure 4(a). With the increase of long-range pairing distance, the area of sensitive CNs becomes larger and larger as depicted in figures 4(b) and (c).

To verify the topological nature of the TSCs, we construct a tight-binding model for an infinitely long strip of $NbSe_2$ with finite width 800 along zigzag and armchair edges (figure 1(a)). Figures 5 and 6 show the energy spectra of zigzag and armchair edge ribbons under mixed superconducting states, respectively. Our calculations demonstrate mismatch between sensitive CNs and corresponding TESs, as shown in figures 5(c),(d), (i), (j) and 6(c), (d), (i), (j). As p_{A1} increases, the correspondence of CNs and TESs of the studied system undergoes three stages: from matching to mismatching, then to mix matching with mismatching. Here, we mainly focus on the TSC phases of fixed CN = −2 and 3 with corresponding $\mu \sim 0.636$ and −0.272 eV near E_F (table 1).

In the first stage, the whole phase diagram consists of the TSC phases with CNs (0, −1, −2, 3). The pairing percentage varies from 1.00⊕0.00–0.84⊕0.16 for the TSC phase with CN = 3 and from 1.00⊕0.00–0.88⊕0.12 for the TSC phase with CN = −2, which indicates that TESs in the CN = −2 TSC phase are more susceptible compared to CN = 3. The CNs are equal to the number of TESs on zigzag and

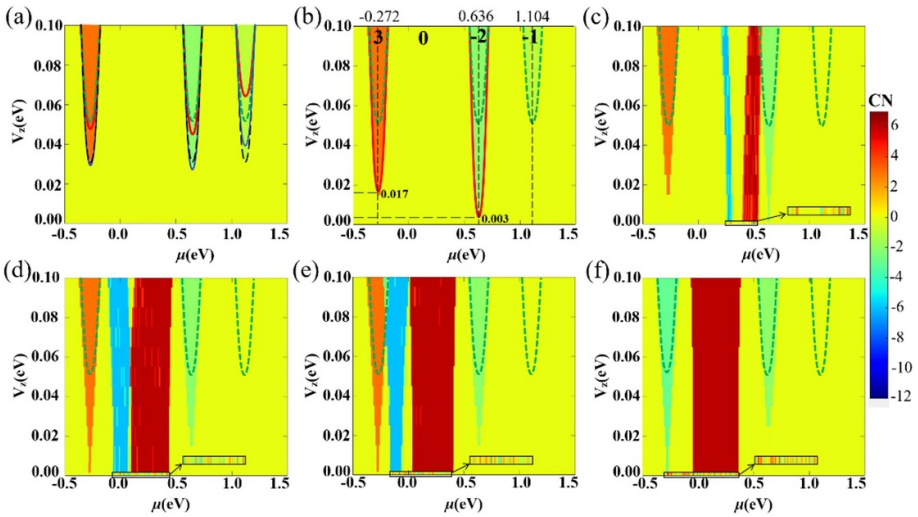

Figure 2. The TSC phase diagrams of $NbSe_2$ with different percent mixed pairing of *s*-wave Δ_s and Δ_{A1_NN}. The green (black) dashed lines represent the TSC phases with pure *s*-wave paring $\Delta_s = 0.05$ (0.03). The red (blue) solid lines represent the TSC phases with total mixed paring $\Delta_t = 0.05$ (0.03). The mixed percentages are: (a) 0.980⊕0.020; (b) 0.860⊕0.140 (the first critical proportion); (c) 0.840⊕0.160; (d) 0.820⊕0.180; (e) 0.812⊕0.188; (f) 0.800⊕0.200 (the second critical proportion). The black boxes pointed by the arrows are enlargements of the TSC phases at zero magnetic field in (c)–(f). The CN is represented by the color scale on the right, the same below.

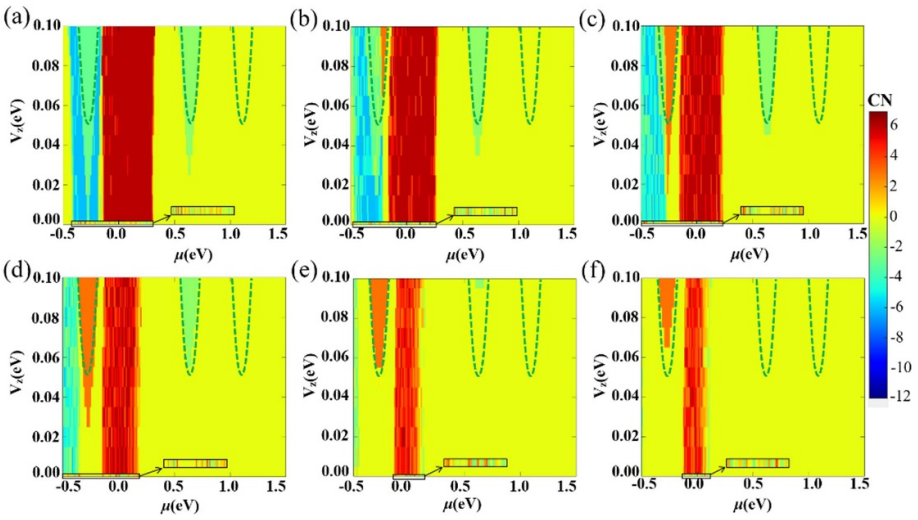

Figure 3. The TSC phase diagrams of $NbSe_2$ with mixed pairing of *s*-wave Δ_s and Δ_{A1_NN}. The TSC phases with fixed and negative sensitive CNs disappear gradually. The green dashed lines represent the TSC phases with pure *s*-wave paring $\Delta_s = 0.05$. The mixed percentages are: (a) 0.780⊕0.220, (b) 0.760⊕0.240, (c) 0.740⊕0.260, (d) 0.700⊕0.300, (e) 0.600⊕0.400, (f) 0.540⊕0.460.

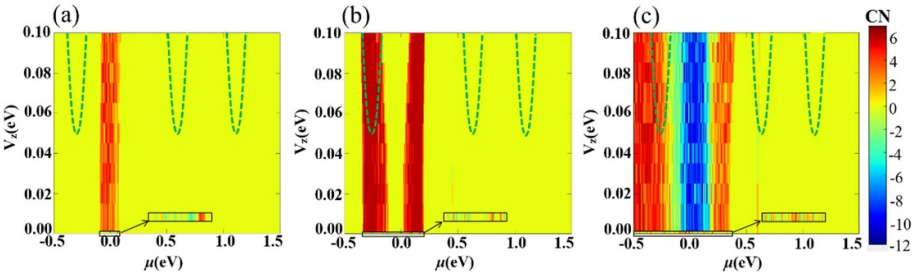

Figure 4. The TSC phase diagrams of $NbSe_2$ with pure Δ_{A1_NN} (a)/ Δ_{A1_NNN} (b)/ Δ_{A1_TNN} (c). The green dashed lines represent the TSC phases with pure *s*-wave paring $\Delta_s = 0.05$.

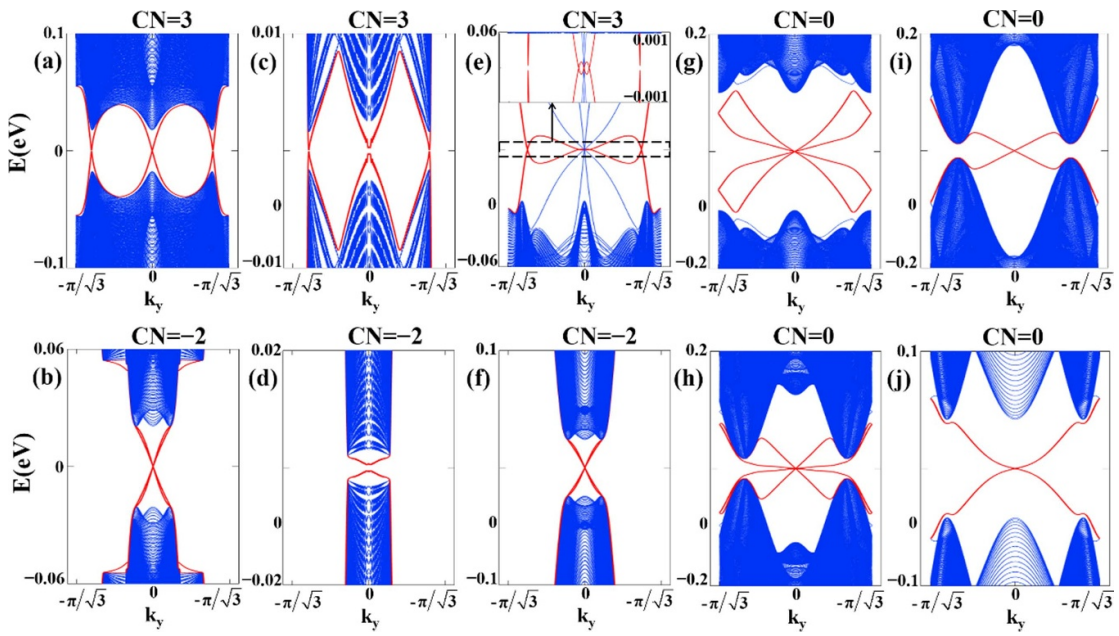

Figure 5. The TESs of zigzag ribbon with 800 unit cells under various mixed pairing of Δ_s and Δ_{A1_NN} with $\alpha_R = 0.1$ eV and different values of V_z and μ. (a)–(h) $V_z = 0.1$ eV and (i)–(j) $V_z = 0.0$ eV. (a)(c)(e)(g) $\mu = -0.272$ eV, (b)(d)(f) $\mu = 0.636$ eV, (h) $\mu = -0.1$ eV, (i) $\mu = -0.5$ eV and (j) $\mu = -0.11$ eV. (a)(b) 0.98⊕0.02, (c) 0.82⊕0.18, (d) 0.86⊕0.14, (e) 0.52⊕0.48, (f) 0.70⊕0.30, (g)–(j) 0.00⊕1.00.

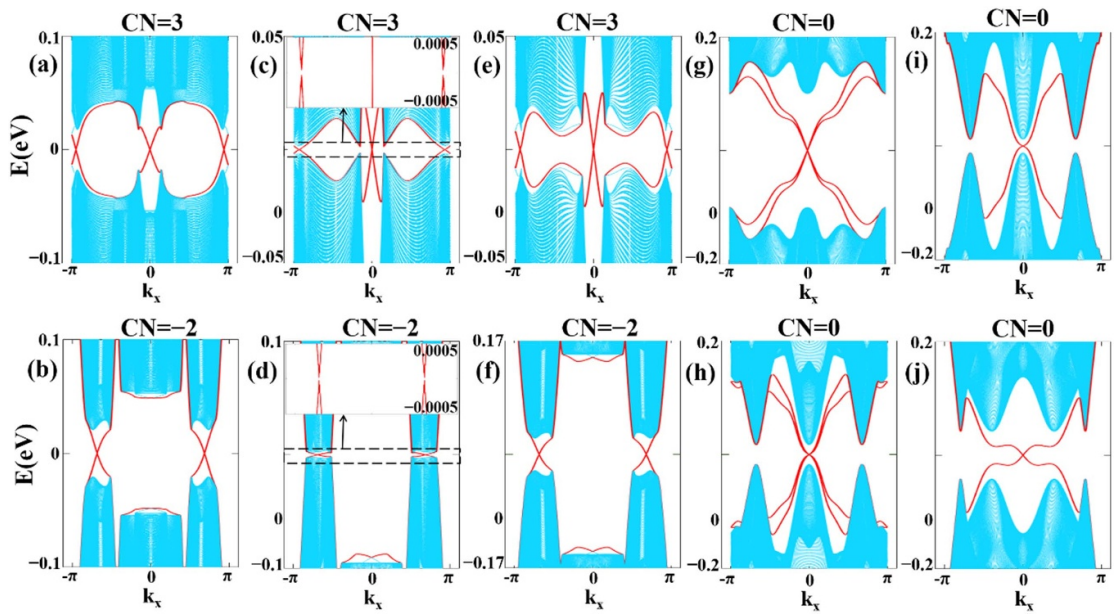

Figure 6. The TESs of armchair ribbon with 800 unit cells under various mixed pairing of Δ_s and Δ_{A1_NN} with $\alpha_R = 0.1$ eV and different values of V_z and μ. (a)–(h) $V_z = 0.1$ eV and (i)–(j) $V_z = 0.0$ eV. (a)(c)(e)(g) $\mu = -0.272$ eV, (b)(d)(f) $\mu = 0.636$ eV, (h) $\mu = -0.1$ eV, (i) $\mu = -0.5$ eV and (j) $\mu = -0.11$ eV. (a)(b) 0.98⊕0.02, (c) 0.82⊕0.18, (d) 0.86⊕0.14, (e) 0.52⊕0.48, (f) 0.70⊕0.30, (g)–(j) 0.00⊕1.00.

Table 1. The correspondence between CNs (3, −2) and TESs under percentages of p_s and NN p_{A1}.

TSC phases with CN = 3			TSC phases with CN = −2		
p_s	p_{A1}	Correspondence	p_s	p_{A1}	Correspondence
1.00–0.84	0.00–0.16	Matching	1.00–0.88	0.00–0.12	Matching
0.83–0.74	0.17–0.26	Mismatching	0.87–0.82	0.13–0.18	Mismatching
0.73–0.42	0.27–0.58	Matching	0.81–0.60	0.19–0.40	Matching

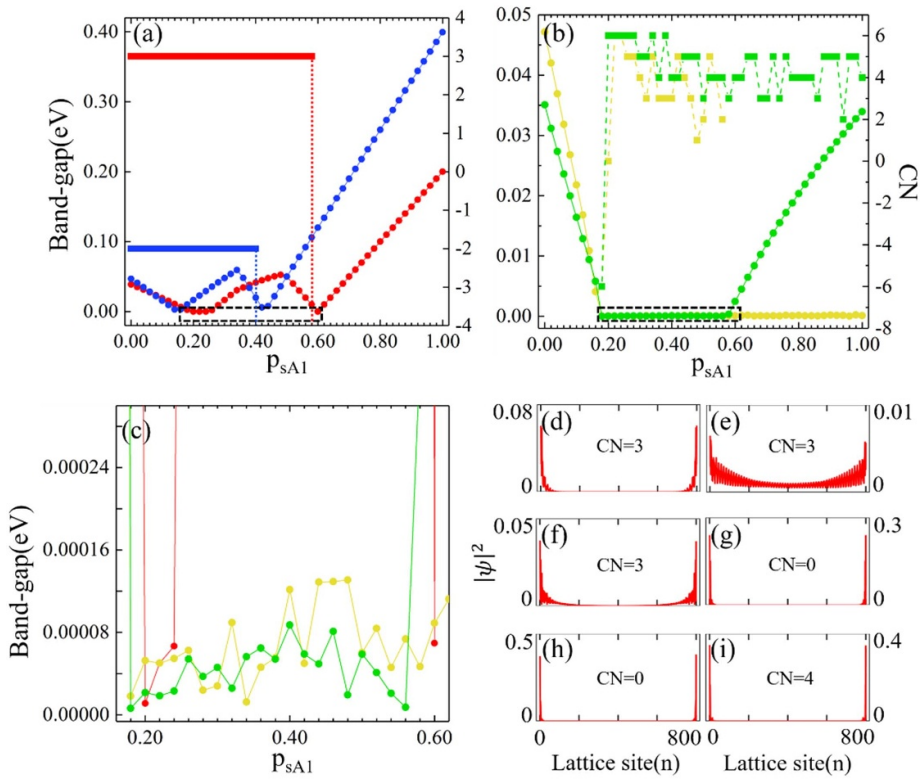

Figure 7. (a)–(b) The bulk band-gap and CNs of different TSCs under $\alpha_R = 0.1$ eV and $V_z = 0.1$ eV. Circles represent the bulk band-gap and squares represent the CNs. Red, blue, green and yellow mark $\mu = -0.272$ eV, 0.636 eV, -0.1 eV, 0.0 eV, respectively. (c) The enlarged bulk band-gap in the black dashed line boxes of (a)(b). (d)–(i) are the $|\psi(n)|^2$ of zigzag ribbon near E_F in real space. (d)–(g) $\mu = -0.272$ eV (d) 0.98⊕0.02, (e) 0.82⊕0.18, (f) 0.70⊕0.30 and (g) 0.00⊕1.00. (h)–(i) 0.00⊕1.00 (h) $\mu = -0.10$ eV and (i) $\mu = 0.00$ eV.

armchair edge ribbons as shown in figures 5(a) and (b) and figures 6(a) and (b), which is in agreement with the normal BBC [2, 37].

In the second stage, the whole phase diagram contains not only fixed CNs ($= -1, -2, 3$), but also sensitive CNs ($= \pm 6, \pm 5, \pm 4, \pm 3, \pm 2, \pm 1$) regions (see figures 2 and 3). The mixed pairing percentage varies from 0.83⊕0.17–0.74⊕0.26 for CN = 3 TSC phases and from 0.87⊕0.13–0.82⊕0.18 for CN = −2 TSC phases. In this stage, the BBC of all TSC phases with topological nonzero CNs is broken (figures 5(c) and (d), figures 6(c) and (d)). The mismatch between CN and TESs may result from the hybrid effect of bulk and edge states due to mini-bulk-band-gap, which will be discussed in detail later. In third stage, fixed CN regions re-match the BBC (figures 5(e)–(h) and 6(e)–(h)), while easy-to-vary CN regions manifest breaking of the BBC.

Compared with the first stage aforementioned, in the third stage, the phase diagram includes simultaneously robust- and fragile-TESs, both are consistent with the BBC as shown in figures 5(e) and (f)/figures 6(e) and (f) and figures 5(h) and (g)/figures 6(h) and (g), respectively. For robust TESs, the edge bands connecting conduction bands and valence bands are nontrivial and not eliminated due to the shifting of the E_F (figures 5(e), (f) and 6(e), (f)). For fragile-TESs, the bands connect the conduction/valence bands themselves or form isolated in-gap bands, therefore can be easily removed by changing the E_F or a continuous perturbation as depicted in figures 5(h), (g) and figures 6(h), (g). Noteworthy, at $V_z = 0$, the TESs for 0.00⊕1.00 state (see figures 5(i), (j) and 6(i), (j)) exhibit robustness, which verifies the above TSC phase diagrams and facilitates experimental detection and the development of TESs-based topological quantum computation [7].

The proximity effect between topological insulators and superconductors induces TSC phases [38–43]. However, there are non-zero energy edge states inherited from the topological insulator in TSCs, affecting CNs and resulting in the mismatch [30]. Therefore, CN can predict the number of TESs crossing the E_F but cannot predict the number of zero-energy Majorana edge states [19]. The closure and opening of bulk band-gap can lead to a topological phase transition [29], while the narrowing and widening of the bulk band-gap can also affect whether the TESs remain clean. We calculate the band-gap between conduction and valance bands to illustrate the effect of the mixed superconducting pairing function on TESs as shown in figures 7(a)–(c). The probability distribution $|\psi(n)|^2$ displays topological superconductivity in real space

near the E_F, as depicted in figures 7(d)–(i). The bulk band-gap of TSC phases with CNs = 3 and −2 oscillates with increasing p_{A1}, leading to the three stages mentioned above between CN and TESs (figure 7(a) and table 1).

In the first stage with NN p_{A1} ∼[0.00, 0.16] and [0.00,0.12], the bulk band-gaps of TSC phases with CNs = 3 and − 2 are larger than ∼0.01 eV orders of magnitude and lead to weak hybrid interaction between the bulk projection states and TESs, consequently demonstrating a good BBC (see figures 5(a) and (e) and figures 6(a) and (e)). The distribution of $|\psi(n)|^2$ is localized dominantly in the both edges of ribbon, as seen in figure 7(d). At the second mismatching stage, the bulk band-gaps are tiny and remain on the order of 10^{-4}eV within the range $p_{A1} = [0.17, 0.26]$ for CNs = 3 and [0.13, 0.18] for CN = −2 TSC phases, respectively (figures 7(a) and (c)). There are many non-topological bulk bands near E_F due to the tiny band-gap, resulting in a large amount of edge projection states. Then the projection states and TESs hybrid strongly and cause the delocalization of TESs, i.e. large values of $|\psi(n)|^2$ on the whole ribbon (figure 7(e)), and consequently breaking the BBC. The distribution of $|\psi(n)|^2$ shows an oscillating behavior with relatively high-amplitude from the edge to the center of ribbon (see figure 7(e)) compared with the localization feature of TESs in the first stage (see figure 7(d)). The oscillating behavior is generally originated from the interference between bulk states and TESs [44]. However, the bulk band-gap re-increases and reaches its maximum at $p_{A1} = 0.40$ for CN = 3 and $p_{A1} = 0.34$ for CN = −2 TSC phases, with the increase of p_{A1} at the third matching stage. It is accompanied by a gradual reduction in non-topological bands near E_F and TESs re-emerge and $|\psi(n)|^2$ re-localizes (see figures 7(f)–(i)), although the band-gap varies.

4. Conclusions

In summary, we systematically investigate TSCs in monolayer $NbSe_2$ by considering various proportions of novel mixed pairing Δ_s and Δ_{A1} based on a tight-binding model. With the increase in the distance and percentage of long-range pairing, the total pairing gap gradually decreases. Firstly, for mixed superconducting pairing states, we observe rich phases with fixed and susceptible CNs as the chemical potential μ and out-of-magnetic field V_z change. The TSC phase manifests matching and mismatching features in relation to the existence of a BBC as p_{A1} increasing. Secondly, the results clearly demonstrate a significant reduction in the critical V_z required to induce TSC phases due to the long-range pairing Δ_{A1}. Intriguingly, the TSC phases can be modulated at $V_z = 0$ under appropriate μ and p_{A1} (when p_{A1} is greater than or equal to 0.16). Moreover, the reality of TSC phase at $V_z = 0$ is further verified by calculating the robust TESs along zigzag and armchair ribbons. Thirdly, it is demonstrated that the CNs do not always match with the number of TESs resulting from the hybrid effect of bulk state and edge state, as evidenced by calculating the bulk band-gap as a function of p_{A1}. It becomes evident that bulk state hybridizes with edge state when the band-gap is tiny, leading to a mismatch between CNs and TESs. Finally, by calculating probability distribution $|\psi(n)|^2$ along ribbon sites, it is found that TESs are localized at the boundary for a matching BBC. However, there is an oscillating behavior of slow decay with the lattice sites for the mismatching/broken BBC. The TSC predicted here can be achieved by applying compressive strain to strengthen long-range pairing in real systems [45–47]. Our investigation provides a new idea and an easier way for the design and regulation of TSC materials in experiment, as well as a theoretical guidance for the fabrication of TSC quantum devices.

Data availability statement

The data cannot be made publicly available upon publication because no suitable repository exists for hosting data in this field of study. The data that support the findings of this study are available upon reasonable request from the authors.

Acknowledgments

This work is supported by the National Natural Science Foundation of China (Grant Nos. 12374046 and 11204261), a Key Project of the Education Department of Hunan Province (Grant No. 19A471), Natural Science Foundation of Hunan Province (Grant No. 2018JJ2381).

ORCID iD

Y Z Li https://orcid.org/0000-0001-8056-2684

References

[1] Nayak A K, Steinbok A, Roet Y, Koo J, Margalit G, Yan B, Oreg Y, Avraham N and Beidenkopf H 2021 Visualization of topological boundary modes manifesting topological nodal-point superconductivity *Phys. Rev.* B **104** 205117

[2] Qi X-L and Zhang S-C 2011 Topological insulators and superconductors *Rev. Modern Phys.* **83** 1057–110

[3] Zhong-Bo Y 2019 Higher-order topological insulators and superconductors *Acta Phys. Sin.* **68** 226101

[4] Qiu D, Gong C, Wang S, Zhang M, Yang C, Wang X and Xiong J 2021 Recent advances in 2D superconductors *Adv. Mater.* **33** 2006124

[5] Sigrist M and Ueda K 1991 Phenomenological theory of unconventional perconductivity *Rev. Mod. Phys.* **63** 239–311

[6] Sato M and Ando Y 2017 Topological superconductors: a review *Rep. Prog. Phys.* **80** 076501

[7] Lian B, Sun X-Q, Vaezi A, Qi X-L and Zhang S-C 2018 Topological quantum computation based on chiral Majorana fermions *Proc. Natl Acad. Sci.* **115** 10938–42

[8] Liu Y *et al* 2020 Type-II ising superconductivity and anomalous metallic state in macro-size ambient-stable ultrathin crystalline films *Nano Lett.* **20** 5728–34

[9] Yuan N F Q, Mak K F and Law K T 2014 Possible topological superconducting phases of MoS_2 *Phys. Rev. Lett.* **113** 097001

[10] Fang Y *et al* 2019 Discovery of superconductivity in 2M WS_2 with possible topological surface states *Adv. Mater.* **31** 1901942

[11] He W-Y, Zhou B T, He J J, Yuan N F Q, Zhang T and Law K T 2018 Magnetic field driven nodal topological superconductivity in monolayer transition metal dichalcogenides *Commun. Phys.* **1** 40

[12] Zhang H *et al* 2022 Tailored Ising superconductivity in intercalated bulk $NbSe_2$ *Nat. Phys.* **18** 1425–30

[13] Barrera S C D L *et al* 2018 Tuning Ising superconductivity with layer and spin–orbit coupling in two-dimensional transitionmetal dichalcogenides *Nat. Commun.* **9** 1427

[14] Lian C-S, Si C and Duan W 2013 Unveiling charge-density wave, superconductivity, and their competitive nature in two-dimensional $NbSe_2$ *Nano Lett.* **18** 2924–9

[15] Kezilebieke S, Huda M N, Vaňo1 V, Aapro M, Gangul S C, Silveira O J, Głodzik S, Foster A S, Ojanen T and Liljeroth P 2020 Topological superconductivity in a van der Waals heterostructure *Nature* **588** 424–8

[16] Sato M and Fujimoto S 2009 Topological phases of noncentrosymmetric superconductors: edge states, Majorana fermions, and non-Abelian statistics *Phys. Rev.* B **79** 094504

[17] Sau J D, Lutchyn R M, Tewari S and Sarma S D 2010 Generic new platform for topological quantum computation using semiconductor heterostructures *Phys. Rev. Lett.* **104** 040502

[18] Tanaka Y, Sato M and Nagaosa N 2011 Symmetry and topology in superconductors–odd-frequency pairing and edge states *J. Phys. Soc. Japan* **81** 011013

[19] Głodzik S and Sedlmayr N 2023 Quantized thermal Hall conductance and the topological phase diagram of a superconducting bismuth bilayer *Phys. Rev.* B **108** 184502

[20] Crépieux A, Pangburn E, Haurie L, Awoga O A, Black-Schaffer A M, Sedlmayr N, Pépin C and Bena C 2023 Superconductivity in monolayer and few-layer graphene. II. Topological edge states and Chern numbers *Phys. Rev.* B **108** 134515

[21] Alsharari A M and Ulloa S E 2022 Inducing chiral superconductivity on honeycomb lattice systems *J. Phys.: Condens. Matter* **34** 205403

[22] Crawford D, Mascot E, Morr D K and Rachel S 2020 High-temperature Majorana fermions in magnet-superconductor hybrid systems *Phys. Rev.* B **101** 174510

[23] Varona S, Ortiz L, Viyuela O and Martin-Delgado M A 2018 Topological phases in nodeless tetragonal superconductors *J. Phys.: Condens. Matter* **30** 395602

[24] Högl P, Frank T, Kochan D, Gmitra M and Fabian J 2020 Chiral Majorana fermions in graphene from proximity-induced superconductivity *Phys. Rev.* B **101** 245441

[25] Chono H, Takasan K and Yanase Y 2022 Laser-induced topological *s*-wave superconductivity in bilayer transition metal dichalcogenides *Phys. Rev.* B **102** 174508

[26] Lee D-H and Chung C-H 2018 Non-centrosymmetric superconductors on honeycomb lattice *Phys. Status Solidi* B **255** 1800114

[27] Liu X-P, Zhou Y, Wang Y-F and Gong C-D 2016 Multifarious topological quantum phase transitions in two-dimensional topological superconductors *Sci. Rep.* **6** 28471

[28] Liu X-P, Zhou Y, Wang Y-F and Gong C-D 2017 Characterizations of topological superconductors: chern numbers, edge states and Majorana zero modes *New J. Phys.* **19** 093018

[29] Sedlmayr N, Kaladzhyan V, Dutreix C and Ben C 2017 Bulk boundary correspondence and the existence of Majorana bound states on the edges of 2D topological superconductors *Phys. Rev.* B **96** 184516

[30] Xiao J, Hu Q, Zeng H and Luov X 2022 The Z_2 topological invariants in 2D and 3D topological superconductors without time reversal symmetry (arXiv:2203.01702)

[31] Christian P, Hanke W and Thomale R 2013 Functional renormalization group for multi orbital Fermi surface instabilities *Adv. Phys.* **62** 453–562

[32] Fukui T, Hatsugai Y and Suzuki H 2005 Chern numbers in discretized brillouin zone: efficient method of computing (Spin) Hall conductances *J. Phys. Soc. Japan* **74** 1674–7

[33] Liu G-B, Shan W-Y, Yao Y, Yao W and Xiao D 2013 Three-band tight-binding model for monolayers of group-VIB transition metal dichalcogenides *Phys. Rev.* B **88** 085433

[34] Sticlet D and Morari C 2019 Topological superconductivity from magnetic impurities on monolayer $NbSe_2$ *Phys. Rev.* B **100** 075420

[35] Dong W-H, Zhang Y-Y, Zhang Y-F, Sun J-T, Liu F and Du S 2022 Superconductivity and topological aspects of two-dimensional transition-metal monohalides *njp Comput. Mater.* **8** 185

[36] Liu C *et al* 2018 Two-dimensional superconductivity and topological states in $PdTe_2$ thin films *Phys. Rev. Mater.* **2** 094001
[37] Hasan M Z and Kane C L 2010 Colloquium: topological insulators *Rev. Modern Phys.* **82** 3045–67
[38] Fu L and Kane C L 2008 Superconducting proximity effect and majorana fermions at the surface of a topological insulator *Phys. Rev. Lett.* **100** 096407
[39] Banerjee A, Sundaresh A, Ganesan R and Kumar P S A 2018 Signatures of topological superconductivity in bulk-insulating topological insulator $BiSbTe_{1.25}Se_{1.75}$ in proximity with superconducting $NbSe_2$ *ACS Nano* **12** 12665–72
[40] Lababidi M and Zhao E 2011 Microscopic simulation of superconductor/topological insulator proximity structures *Phys. Rev.* B **83** 184511
[41] Sun H-H and Jia J-F 2017 Majorana zero mode in the vortex of an artificial topological superconductor *Sci. Chin.* **60** 057401
[42] Zhang P *et al* 2018 Observation of topological superconductivity on the surface of an iron-based superconductor *Science* **350** 182–6
[43] Wang M-X *et al* 2012 The coexistence of superconductivity and topological order in the Bi_2Se_3 thin films *Science* **336** 52–55
[44] Li Z-X, Cao Y and Yan P 2021 Topological insulators and semimetals in classical magnetic systems *Phys. Rep.* **915** 1–64
[45] Zollner K, Junior P E F and Fabian J 2019 Strain-tunable orbital, spin-orbit, and optical properties of monolayer transition-metal dichalcogenides *Phys. Rev.* B **100** 195126
[46] Inbar H S *et al* 2023 Tuning the band topology of GdSb by epitaxial strain *APL Mater.* **11** 111106
[47] Sclauzero G and Ederer K D C 2016 Tuning the metal-insulator transition in d^1 and d^2 perovskites by epitaxial strain: a first-principles-based study *Phys. Rev.* B **94** 245109